Reference Solutions for Benchmark Turbulent Flows in Three Dimensions

Boris Diskin,*
National Institute of Aerospace, Hampton, VA 23666

James L. Thomas,† Mohagna J. Pandya,‡ Christopher L. Rumsey,§
NASA Langley Research Center, Hampton, VA 23681

A grid convergence study is performed to establish benchmark solutions for turbulent flows in three dimensions (3D) in support of turbulence-model verification campaign at the Turbulence Modeling Resource (TMR) website. The three benchmark cases are subsonic flows around a 3D bump and a hemisphere-cylinder configuration and a supersonic internal flow through a square duct. Reference solutions are computed for Reynolds Averaged Navier Stokes equations with the Spalart-Allmaras turbulence model using a linear eddy-viscosity model for the external flows and a nonlinear eddy-viscosity model based on a quadratic constitutive relation for the internal flow. The study involves three widely-used practical computational fluid dynamics codes developed and supported at NASA Langley Research Center: FUN3D, USM3D, and CFL3D. Reference steady-state solutions computed with these three codes on families of consistently refined grids are presented. Grid-to-grid and code-to-code variations are described in detail.

*NIA Research Fellow and Research Associate Professor, MAE Department, University of Virginia, Charlottesville, VA, Associate Fellow AIAA.
†Distinguished Research Associate, Computational AeroSciences Branch, Fellow AIAA.
‡Research Aerospace Engineer, Configuration Aerodynamics Branch, Senior Member AIAA.
§Senior Research Scientist, Computational AeroSciences Branch, Fellow AIAA.

I. Introduction

The Turbulence Modeling Resource (TMR) website[1,2] established at NASA Langley Research Center has been widely used to verify and validate turbulence models. Validation cases offered at this website compare numerical solutions of specific turbulence models with well-documented experimental measurements and assess the modeling error associated with model equations. The results of validation tests intend to establish the ability of model equations to represent physics in a particular flow regime. Verification tests focus on solution-to-solution comparisons and serve to avoid ambiguity and establish correctness of specific implementations of turbulence models in computational fluid dynamics (CFD) codes.

More recently, a section "Cases and Grids for Turbulence Model Numerical Analysis" has been added to the TMR website. The test cases in this section are designed primarily for numerical analysis of solver technology used in turbulent flow simulations; e.g., grid and iterative convergence properties, effects of specific discretizations, grid-refinement strategies, etc. In support of the TMR objectives, two special sessions on solver technology for Reynolds-Averaged Navier Stokes (RANS) equations were held at the AIAA Science and Technology Forum and Exposition (SciTech) 2015. Advanced solver technologies for RANS equations with a one-equation linear eddy-viscosity Spalart-Allmaras (SA) turbulence model[3,4] were presented. The technologies were demonstrated in application to two relatively simple benchmark flows in two dimensions (2D), namely, subsonic turbulent flows around a flat plate configuration and a NACA 0012 airfoil. For these benchmark flows, the reference solutions were computed by three well established CFD codes, FUN3D (NASA), CFL3D (NASA), and TAU (DLR), on families of consistently refined grids that included grids with up to 15 millions degrees of freedom. Detailed descriptions of the reference solutions have been posted on the TMR website.

This paper extends the previous study by considering to three dimensions (3D). Reference steady-state RANS solutions are computed for three benchmark turbulent flows proposed at the TMR website: a subsonic flow around a 3D bump, a subsonic flow around a hemisphere-cylinder configuration and a supersonic flow through a square duct. The first two cases use the SA-neg[4] variant of the SA model, which allows negative values for the Spalart turbulence variable. The SA-neg model is one of linear eddy viscosity models based on the Boussinesq assumption. The third case uses a variation of the SA model with Quadratic Constitutive Relation (QCR),[5] which is termed at TMR as SA-QCR2000. The QCR extension is important to account for anisotropies in turbulent stresses that cannot be captured with models based on the Boussinesq assumption. Families of grids satisfying the current guidelines for grid convergence studies[6,7] are used. Three of NASA's CFD solvers are used in this study: FUN3D, USM3D, and CFL3D. These codes use different discretization and iteration schemes. To exclude the influence of iterative errors, all three codes converge residuals on all grids to near machine-zero levels.

The material in the paper is presented in the following order. First, the codes used in the current study are briefly described in Section II, including discretization details and iterative convergence strategies. Then, benchmark turbulent solutions for a subsonic flow around a 3D bump are described in Section III. Solutions with the SA-neg model on a family of consistently refined grids with each of the three codes are compared. Section IV reports grid convergence studies for a subsonic flow around a hemisphere-cylinder configuration at zero angle of attack. Solutions with the SA-neg model from the three codes on two different grid families are compared with each other and with experimental measurements. FUN3D and USM3D solutions with the SA-QCR2000 turbulence model for a supersonic flow through a square duct are presented in Section V. Finally, concluding remarks are offered in Section VI.

II. CFD Codes Used in the Study

This section describes three well-established practical CFD codes used in this study. The codes developed and supported by NASA are widely used by US government, industry, and academia and represent the state of the art in aerodynamic computations.

A. FUN3D

FUN3D is a finite-volume, node-centered, unstructured-grid RANS solver, which is widely used for high-fidelity analysis and adjoint-based design of complex turbulent flows.[8–15] FUN3D solves the governing flow equations on mixed-element grids; the elements are tetrahedra, pyramids, prisms, and hexahedra. At median-dual control-volume faces, the inviscid fluxes are computed using an approximate Riemann solver. Roe's flux difference splitting (FDS) is used in the current study. For second-order accuracy, face values are obtained by a MUSCL scheme, with unweighted least-squares gradients computed at the nodes. There are options to use a directional gradient along the grid lines

and/or the approximate mapping (AM) method[16–18] that maps the interior nodes to the viscous surface using the distance function. For this study, the MUSCL scheme coefficient is set to $\kappa = 0.5$ for the meanflow equations.

The viscous fluxes use full approximation of viscous stresses. For tetrahedral meshes, the viscous fluxes are discretized using the Green-Gauss (cell-based) gradients; this is equivalent to a Galerkin type approximation. For non-tetrahedral meshes, the edge-based gradients are combined with Green-Gauss gradients; this improves the h-ellipticity of the viscous operator. The diffusion term in the turbulence model is handled in the same fashion as the meanflow viscous terms. FUN3D uses the SA-neg variant[4] of the SA turbulence model[3] that admits negative values for the Spalart turbulence variable. This variant was designed for improved numerical behavior. The SA-neg model is identical to the original SA model for positive values of the Spalart turbulence variable. For QCR terms, FUN3D employs the SA-QCR2000 formulation.[5] In these studies, FUN3D uses a first-order approximation for the convection term in the turbulence-model equation.

To solve nonlinear flow equations, FUN3D uses a hierarchical nonlinear iterative method (HANIM). On the innermost level HANIM uses a preconditioner based on a defect-correction method and iterates on a simplified first-order Jacobian with a pseudo-time term. One preconditioner iteration involves a point- or line-implicit multi-color pass through the domain. The number of preconditioner iterations may vary for different nonlinear iterations. A Generalized Conjugate Residual (GCR) method uses the preconditioner solutions to converge linear residuals and to compute solution correction. A nonlinear controller assesses the correction computed by the linear solver. The controller is responsible for the CFL adaptation strategy and for deciding when to update the Jacobian. As a result of this assessment, the suggested correction can be applied fully, partially, or completely discarded; the current Jacobian may be updated or reused in the next iteration; and the current CFL number may increase, decrease, or stay the same. The nonlinear iterations can be tightly or loosely coupled, i.e., operate on the meanflow and turbulence equations collectively or separately. Initially, the CFL number is ramped over a prescribed number of iterations, but then it automatically changes within prescribed bounds.

B. USM3D

USM3D is an unstructured finite-volume cell-centered RANS solver[19] that has been widely used within NASA,[20,21] other U.S. government agencies,[22] and industry[23] as a workhorse for aerodynamic analysis of complex configurations. The enhanced mixed-element version of USM3D[24,25] is used for this study. A fully-implicit formulation is implemented implying that the auxiliary solution variables at the grid nodes and boundary faces as well as the cell gradients are computed solely from the current solution variables defined at the cell centers. Solution values at the nodes are averaged from solutions at surrounding cells using a pseudo-Laplacian method,[26–29] which is equivalent to a least-squares minimization procedure with a linear fit.[30] The second-order spatial discretization of inviscid fluxes is accomplished by reconstructing solutions at the cell faces; the reconstruction is based on solution gradients computed within cells. The reconstruction scheme corresponds to the MUSCL scheme with $\kappa = 0.0$. For this study, the cell gradients are evaluated with the Green-Gauss integration using solution values at the nodes. Inviscid fluxes are computed at each cell face using the upwind Roe's FDS scheme. Face gradients required for evaluation of viscous fluxes are computed from the Mitchells stencil.[31,32] The SA-neg[4] and SA-QCR2000[5] variants of the SA model[3] are used in this study. The convective term of the SA turbulence model equation is approximated with the first-order accuracy. The velocity gradients contributing to the source term of the SA model are computed at cell centers using the face area average of face gradients. In the presence of grid lines, accuracy of the velocity gradients is improved by augmentation with a directional gradient based on the line mapping.

A HANIM solver described in an accompanying paper[25] is used for nonlinear iterations. The USM3D preconditioner uses a defect correction scheme. The approximate Jacobian for the mean flow equations is formed using the linearization of the first-order FDS inviscid fluxes and a thin-layer approximation for the viscous fluxes. The approximate Jacobian for a turbulence-model equation includes the contributions from the advection, diffusion, and source terms. The advection term is linearized with a first-order approximation. A thin-layer approximation is used for the diffusion term. The entire contribution from the linearized source term is added to the diagonal. Positivity check for the diagonal values is conducted before adding the pseudo-time term. Negative diagonal values are substituted by their absolute values. An option to use single precision for the approximate Jacobian off-diagonal terms and for the solution updates is available to reduce the memory footprint.

The preconditioner equations are solved with point- or line-implicit Gauss-Seidel (G-S) iterations. The mean flow and turbulence model preconditioner G-S iterations are loosely coupled. Residual reduction targets are used for an earlier termination of G-S iterations to improve the runtime efficiency. HANIM uses CFL adaptation as a comprehensive tool to improve robustness and efficiency of nonlinear iterations. It provides two additional hierarchies over the USM3D preconditioner solver. The hierarchies are an enhanced linear solver for the exact linearization

of RANS equations and a nonlinear control of the solution update. The linear solver uses GCR-based matrix-free methods, couples residuals of the meanflow and turbulence model equations, and is expected to meet certain residual reduction targets. The nonlinear solution update strategy automatically checks solution realizability (positive pressure and density) at cell centers and adapts the under-relaxation parameter and pseudo-time step.

C. CFL3D

CFL3D is a structured-grid multiblock cell-centered finite-volume code widely applied for analysis of complex flows. It has been used in many recent workshops involving complex turbulent flows[8,33–35] and for computing benchmark turbulent-flow solutions at the TMR website. It uses second-order, upwind-biased spatial differencing scheme (a MUSCL scheme[36,37] corresponding to $\kappa = 1/3$ that allows a third-order accuracy in one dimension for the convective and pressure terms, and second-order differencing for the viscous terms; it is globally second-order accurate. Roe's FDS method is used to obtain inviscid fluxes at the cell faces. The option to model the full Navier-Stokes meanflow equations is exercised for all cases. CFL3D uses the SA-neg scheme[4] to model eddy viscosity. In distinction from the other two codes that use a first-order approximation for the convection term in the SA model, CFL3D uses a second-order approximation in this study. The turbulence-model diffusion term uses the thin-layer approximation. The iteration scheme is loosely coupled, i.e., first, the meanflow equations are advanced with the eddy-viscosity fixed, then the turbulence-model equation is advanced with the meanflow solution fixed. CFL3D employs local time-step scaling, grid sequencing, and multigrid to accelerate convergence to steady state.

III. Subsonic Flow over Bump

A grid convergence study for a subsonic turbulent flow around a 3D bump configuration is presented in this section. This test case corresponds to the 3D Modified Bump case in the "Cases and Grids for Turbulence Model Numerical Analysis" section of the TMR website. The goal of this study is to establish an accurate reference solution for a non-trivial 3D configuration that can be used for verification of RANS solvers with the SA turbulence model.

A. Geometry, Boundary Conditions, and Flow Parameters

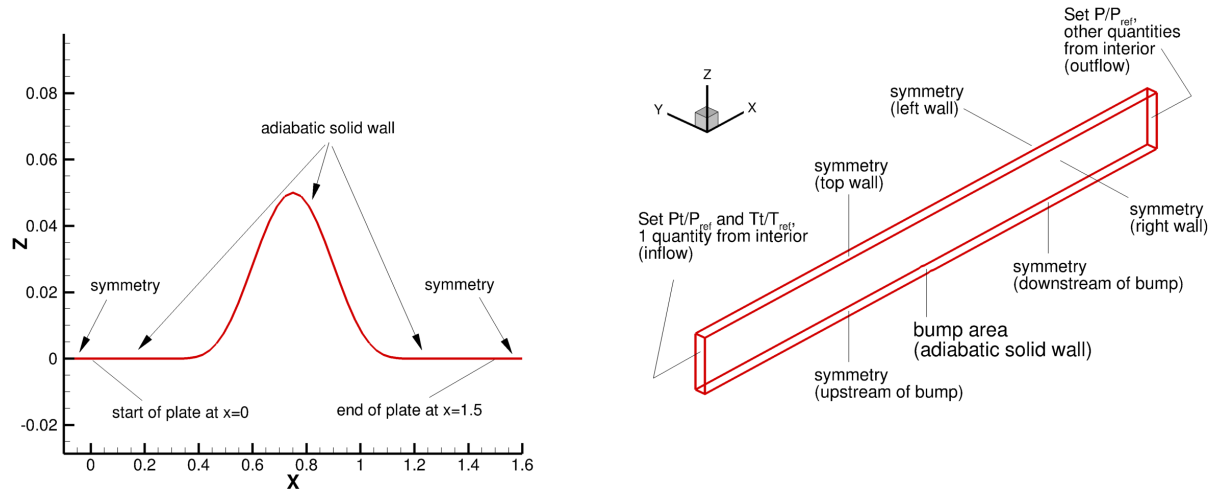

(a) 2D bump profile.

(b) 3D bump layout.

Figure 1. Bump boundary conditions.

The 3D bump geometry is derived from a 2D bump profile

$$\begin{cases} z = 0.05\left(\sin\left(\frac{\pi x}{0.9} - \frac{\pi}{3}\right)\right)^4, & 0.3 \le x \le 1.2, \\ z = 0, & 0 \le x < 0.3 \quad \text{and} \quad 1.2 < x \le 1.5. \end{cases} \tag{1}$$

Here, z is the vertical direction and x is the streamwise direction. The body reference length is 1.5 units, while the actual bump corresponding to $z > 0$ is at $0.3 < x < 1.2$. The maximum bump height $\max(z) = 0.05$.

In the 3D setting, the 2D profile is defined along the line $y = 0$. A spanwise (y-directional) variation is added as

$$x = x_0 + 0.3\left(\sin\left(\pi y\right)\right)^4, \qquad -0.5 \leq y \leq 0, \tag{2}$$

where x_0 is any given location on the 2D profile, Eq. 1.

The boundary conditions are defined as follows. Adiabatic no-slip solid-wall boundary conditions are set on the bump surface, Eqs. 1 and 2. The upstream and downstream farfield boundary conditions are set at $x = -25$ and $x = 26.5$, respectively. Constant total pressure and total temperature boundary conditions corresponding to $P_t/P_{ref} = 1.02828, T_t/T_{ref} = 1.008$ are applied at the upstream boundary, and constant pressure boundary conditions corresponding to $P/P_{ref} = 1$ are applied at the downstream boundary. Symmetry boundary conditions are imposed on the bottom boundary at $z = 0$ between the farfield and the solid wall ($-25 < x < 0.3\left(\sin\left(\pi y\right)\right)^4$ and $1.5 + 0.3\left(\sin\left(\pi y\right)\right)^4 < x < 26.5$), on the top boundary at $z = 5.0$, and on the side walls set at $y = 0$ and $y = -0.5$. Figures 1 (a) and (b) show the close-up view of the 2D profile at $y = 0$ and the layout of the 3D boundary conditions, respectively.

A subsonic ($M_{ref} = 0.2$) compressible turbulent flow is considered. The Reynolds number computed per unit length is $Re = 3\text{M}$. The freestream static temperature is $T_{ref} = 540°$ Rankine. The farfield value of the Spalart turbulence variable is $\tilde{\nu}_{farfield} = 3\nu_\infty$. The Prandtl number is taken to be constant at $Pr = 0.72$, and the turbulent Prandtl number is taken to be constant at $Pr_t = 0.9$. The molecular viscosity is computed using Sutherland's Law.[38]

B. Grids

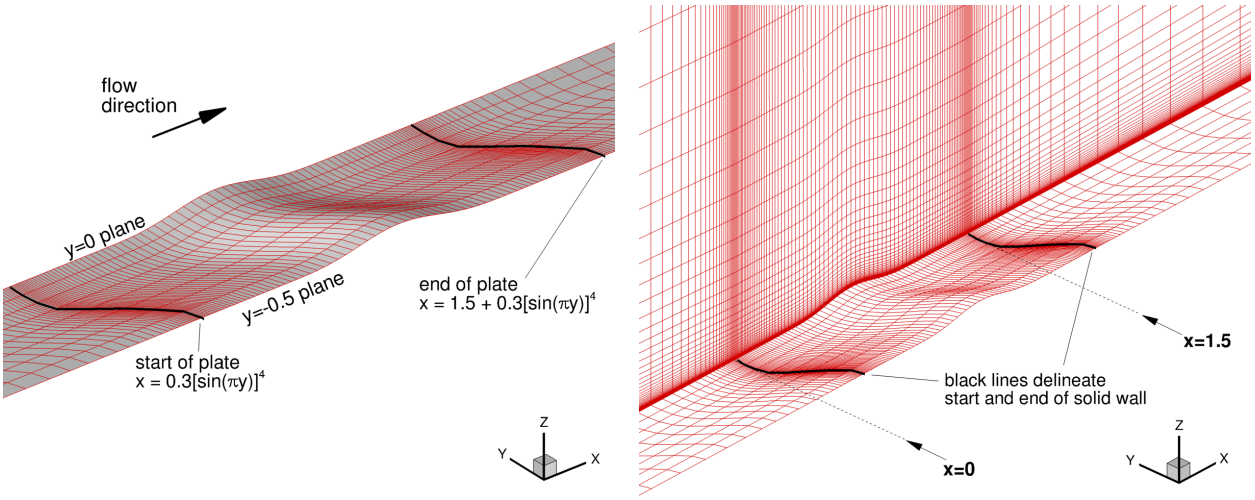

(a) Bump shape.

(b) $9 \times 177 \times 81$ grid.

Figure 2. 3D bump geometry

A family of six nested uniformly refined 3D hexahedral grids has been generated. Within the family, grids have been generated recursively, starting from the finest grid. Each coarser grid in the family is derived from the preceding finer grid by removing every-other grid plane in each dimension. Grids are ranging from the finest $65 \times 1409 \times 641$ grid to the coarsest $3 \times 45 \times 21$ grid. The grid dimensions represent the numbers of nodes in the spanwise, streamwise, and vertical directions, respectively. The finest grid has minimum spacing at the wall of $z = 5.0 \times 10^{-7}$, giving an approximate average $z^+ = 0.06$ over the bump surface. Even the coarsest grid has reasonably fine wall-normal spacing, giving an approximate average $z^+ = 2.0$ over the bump. The grids are stretched in the wall-normal direction and clustered near the leading and trailing edges. The spacing in the spanwise direction is uniform. Figures 2(a) and (b) show the bump surface and a portion of the $9 \times 177 \times 81$ grid.

C. Results

For the 3D bump flow, an odd-even decoupling was observed in FUN3D solutions on finer grids using unweighted least-square gradients for inviscid fluxes. Preliminary studies indicate the decoupling is associated with a degradation of the gradients near the inflection point on the bump surface. The instability occurred even on very coarse grids in solutions with a full Reynolds stress turbulence model. The decoupling was eliminated for either the SA or the full Reynolds stress model by using the AM method[16–18] for inviscid fluxes. The AM method is used for the meanflow inviscid fluxes for the 3D bump case only; FUN3D solutions with unweighted least-square gradients are not shown for this case.

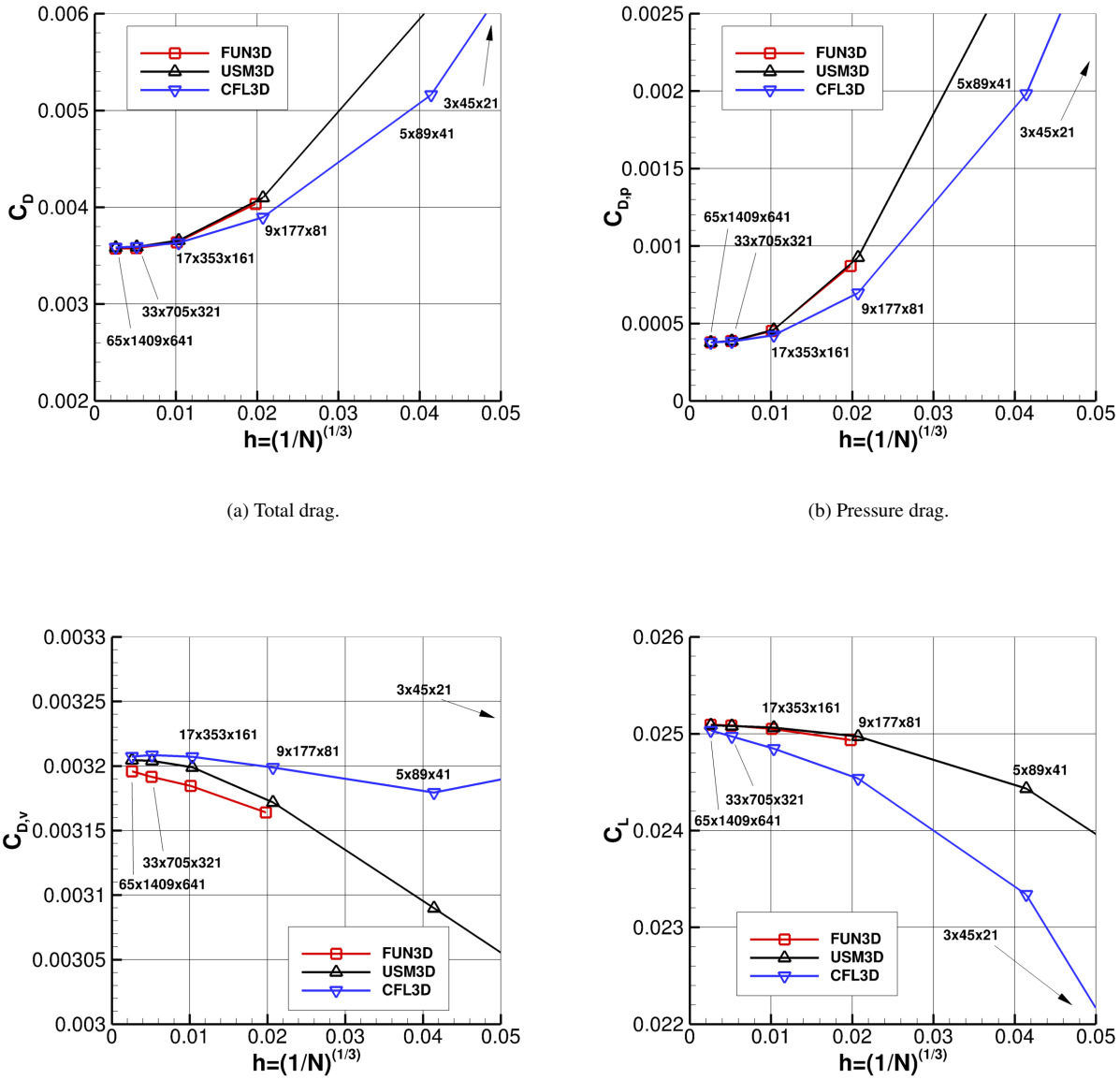

(a) Total drag.

(b) Pressure drag.

(c) Viscous drag.

(d) Lift.

Figure 3. Grid convergence of drag and eddy viscosity

Grid convergence of the total drag, viscous drag, pressure drag, and lift coefficients is shown in Figure 3. The value of the characteristic mesh size, h, is computed as $h = N^{-\frac{1}{3}}$, where N is the number of degrees of freedom (cells for USM3D and CFL3D and nodes for FUN3D). All coefficients appear converging in grid refinement to the

same limit. The code-to-code variation between the drag coefficients computed on the finest grid is less than 0.32% (less than 0.12 drag counts); the corresponding variation of the lift coefficient is less than 0.24%. The viscous drag constitutes about 80% of the total drag computed on the finest grid. The pressure drag sharply decreases in grid refinement, converges with an apparent order that is higher than second, and is largely responsible for the total drag grid-to-grid variation. The viscous drag shows little variation in grid refinement, slowly increasing on finer grids. The apparent order of viscous drag convergence differs between the codes: USM3D apparent order is higher than second, the FUN3D apparent order is first, and the CFL3D convergence direction has changed on the finest grid. The lift coefficient monotonically increases in grid refinement and converges with an apparent order higher than first. Overall, the asymptotic convergence order has not been established. The pressure drag and lift coefficients computed by FUN3D and USM3D are closer to each other than to the corresponding coefficients computed by CFL3D. The viscous drag coefficients computed by USM3D and CFL3D on fine grids are closer to each other than to the corresponding coefficients computed by FUN3D.

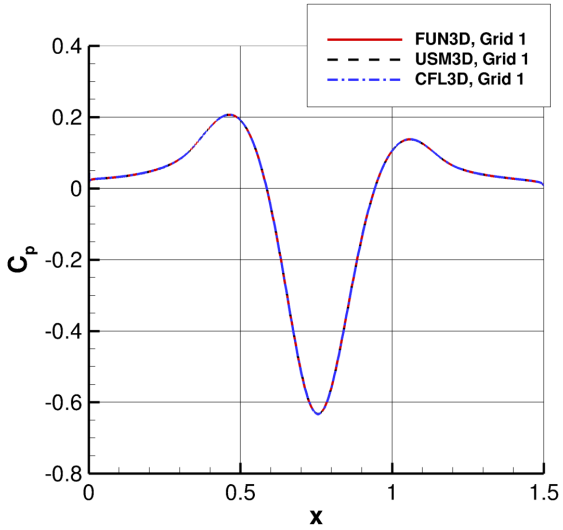

Figure 4. Variation of surface pressure coefficient along the centerline, $y = 0$. Global view.

A global view of the pressure coefficient variation along the viscous surface centerline, $y = 0$, is shown in Figure 4. Only solutions computed on the finest grid in the family are shown. An excellent agreement between the solutions computed by FUN3D, USM3D, and CFL3D is observed. In this global view, all three plots are indistinguishable. Zoomed views of the grid convergence of the centerline pressure variation near the global minimum are shown in Figure 5. All solutions show remarkably similar approaches to the grid converged value of the pressure coefficient. This similarity indicates that, for these particular RANS formulation and flow conditions, differences in grids are by far more important than discretization differences.

Variation of the surface pressure coefficient along the grid line $x = 0.690420848175 + 0.3\left(\sin\left(\pi y\right)\right)^4$ is shown in Figure 6. The grid 4 (and all coarser grids) is too coarse to reasonably represent the surface pressure variation. The surface pressure curves are close to each other on grids 3 to 1. FUN3D shows smallest variation in grid refinement. On the finest grid 1, the three solutions are indistinguishable within the plotting accuracy.

Variations of the velocity components, pressure and eddy viscosity along a vertical line behind the bump corresponding to $x = 1.20791, y = -0.125$ are shown in Figures 7-11. Solutions on four fine grids are shown. Vertical variation of the streamwise velocity component u is shown in Figure 7. The streamwise velocity is smoothly varying and well resolved on all grids. The curves computed on all grids by all codes are indistinguishable. The spanwise and vertical velocity components shown in Figures 8 and 9, respectively, are much smaller and more sensitive to grid resolution. The magnitudes of near-surface spanwise velocity computed on three finest grids are much smaller than the corresponding magnitudes computed on grid 4. The grid-to-grid variation of the vertical velocity is small in CFL3D and FUN3D solutions and is larger in the USM3D solution. The curves of the velocity components computed on the finest grid 1 cannot be distinguished in this view.

Vertical pressure variation is illustrated in Figure 10. FUN3D solutions show remarkably little variation in grid refinement. USM3D and CFL3D solutions exhibit larger pressure on grid 4 than on finer grids. Again, the pressure

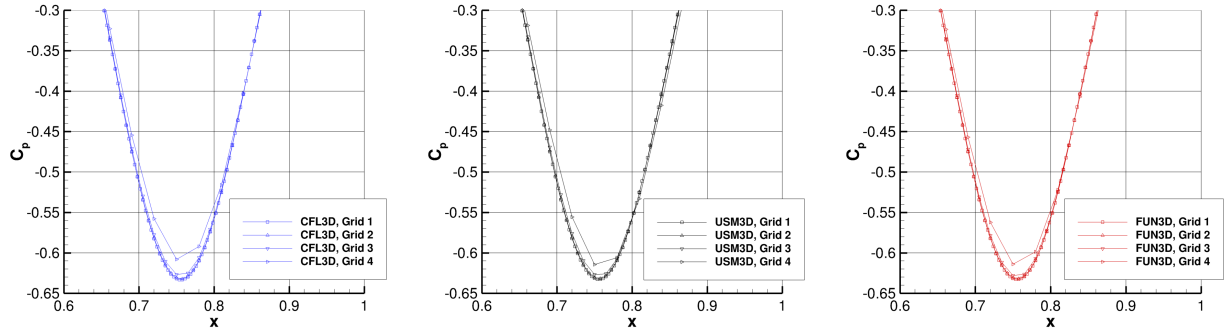

(a) CFL3D. (b) USM3D. (c) FUN3D.

Figure 5. Variation of surface pressure coefficient along the centerline, $y = 0$. Zoomed view.

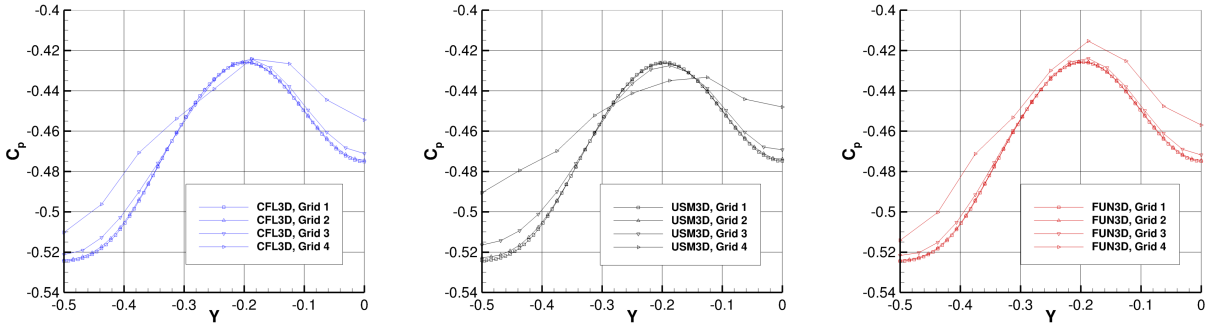

(a) CFL3D. (b) USM3D. (c) FUN3D.

Figure 6. Spanwise variation of surface pressure coefficient

variation in solutions computed on the finest grid 1 is virtually the same for all codes.

Finally, vertical variations of the eddy viscosity are shown in Figure 11. A more significant variation between solutions in grid refinement can be seen in the region near $z \approx 0.23$, where eddy viscosity transitions to zero. This is the only place in all vertical variation plots, where the finest grid 1 solutions are clearly visible, at least in FUN3D and USM3D plots. Eddy viscosity in CFL3D solutions shows less variation in grid refinement. All grid 1 plots are indistinguishably similar.

IV. Subsonic Flow around Hemisphere Cylinder

Reference solutions for a flow around a 3D hemisphere-cylinder configuration is presented in this section. The study corresponds to the case described in 3D Hemisphere Cylinder Validation Case in the Cases and Grids for Turbulence Model Numerical Analysis section of the TMR website. The reference solutions computed by FUN3D, USM3D, and CFL3D, on two families of grids can be used for verification of RANS solvers for a turbulent flow over a smooth 3D body of revolution. A comparison with an experimental study[39] is shown as well and provides a basis for the SA turbulence model validation.

A. Geometry, Boundary Conditions, and Flow Parameters

The geometry is taken from the experimental study reported by Tsieh.[39] In the experiment, the radius of the hemisphere was $0.5in$, the body length was $10in$, and the Reynolds number per foot was $4.2M$. Thus, in the computational

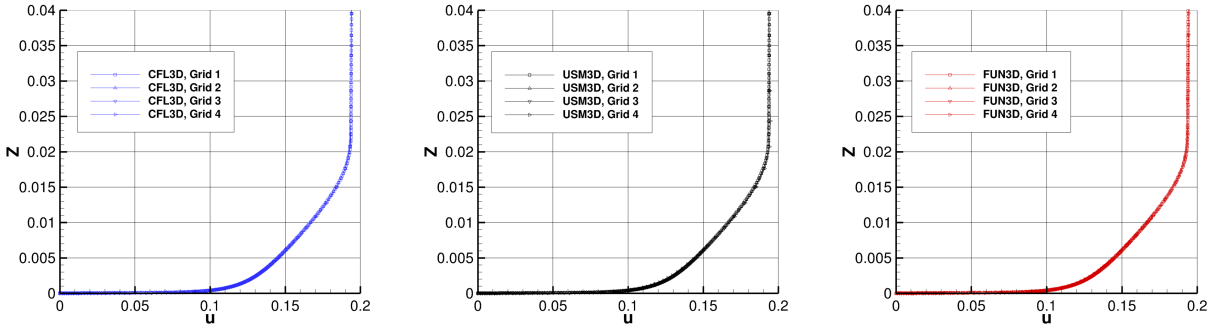

(a) CFL3D. (b) USM3D. (c) FUN3D.

Figure 7. Vertical variation of streamwise velocity component

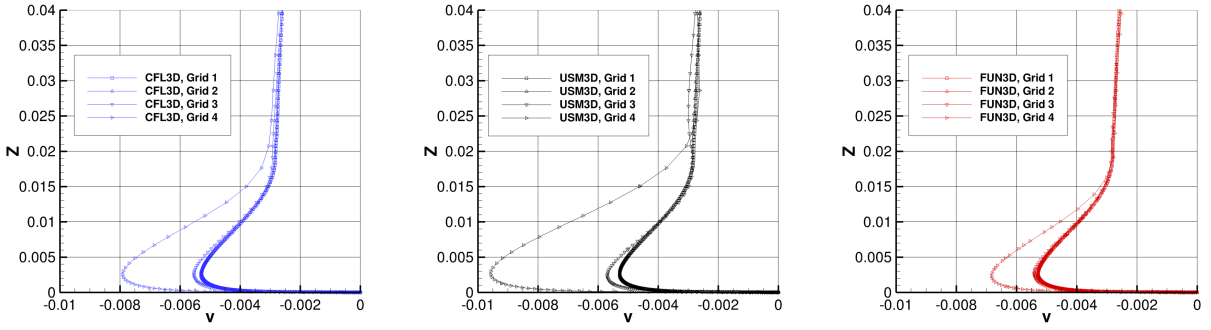

(a) CFL3D. (b) USM3D. (c) FUN3D.

Figure 8. Vertical variation of spanwise velocity component

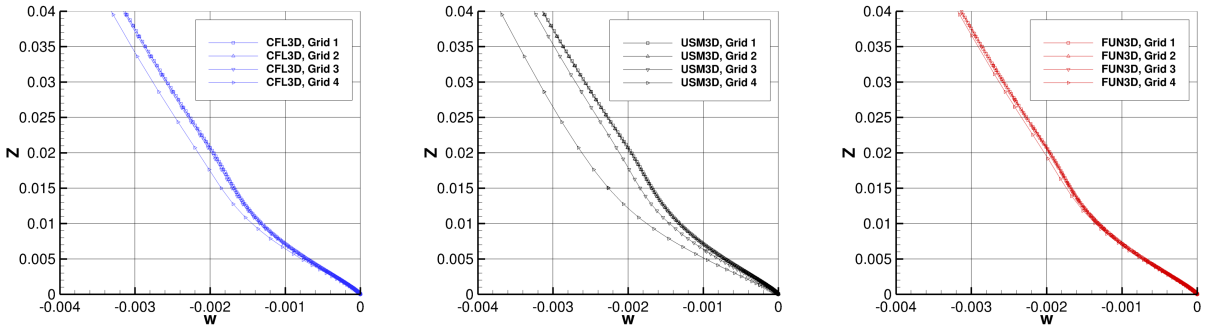

(a) CFL3D. (b) USM3D. (c) FUN3D.

Figure 9. Vertical variation of vertical velocity component

domain with the unit length taken as $1in$, the hemisphere radius is 0.5, the cylinder length is 10, and Reynolds number is $Re = 0.35M$ per unit length. The reference solutions are computed at the following flow conditions: $M_{ref} = 0.6$, angle of attack of $AoA = 0°$, and the reference temperature $T_{ref} = 540°$ Rankine.

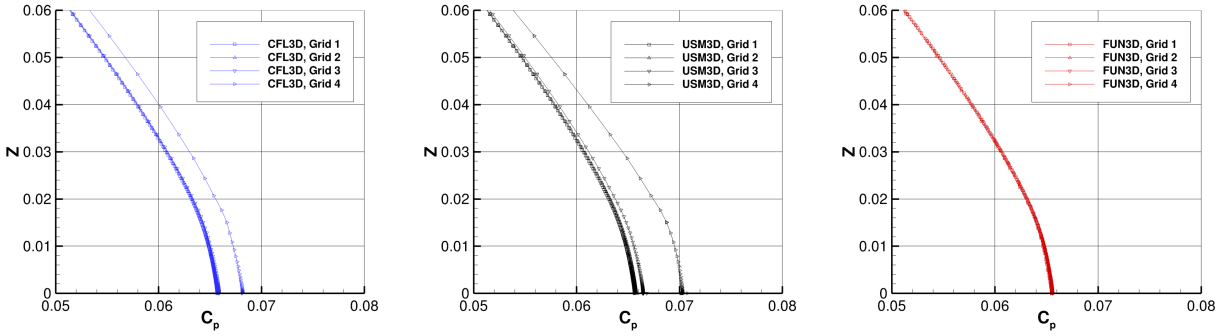

(a) CFL3D. (b) USM3D. (c) FUN3D.

Figure 10. Vertical pressure variation

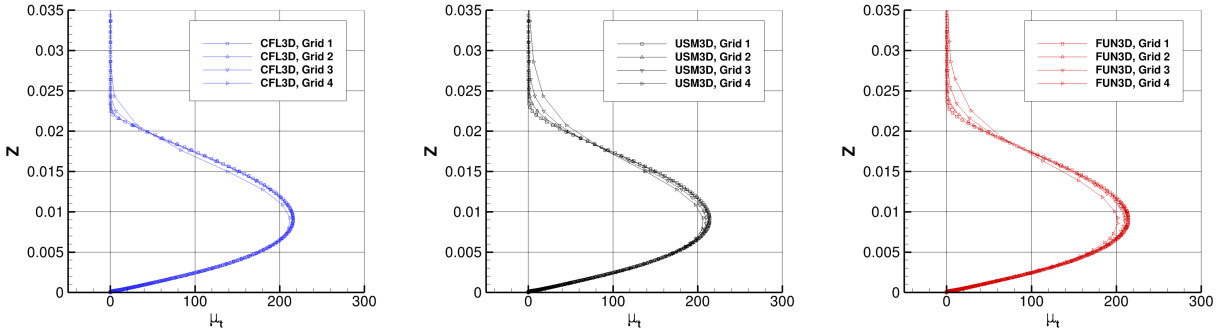

(a) CFL3D. (b) USM3D. (c) FUN3D.

Figure 11. Vertical eddy viscosity variation

The origin of the coordinate system is located at the apex of the hemisphere. The positive x direction is the streamwise direction co-linear with the axis of the hemisphere and cylinder. Figure 12 shows the layouts of boundary conditions for structured and unstructured grid domains. The layouts have different placements of farfield boundary. The unstructured-grid domain (Figure 12 (a)) has the farfield located at an averaged distance of 20 radii from the body; the structured-grid domain (Figure 12 (b)) has the farfield located at 40 radii. The Riemann boundary conditions with the external state taken as the freestream solution at the input Mach number are set at the upstream boundary . The downstream computational boundary is located at the back of the cylinder, $x = -10.5$. The outflow conditions specified at the downstream boundary are constant pressure conditions corresponding to $P/P_{ref} = 1$.

B. Grids

Two families of grids have been generated. A family of three nested unstructured computational grids has been used by FUN3D and USM3D. The grids are designed to avoid polar singularity. Thus, the number of cells sharing a node and the aspect ratio of boundary faces remain bounded as grids are refined. These unstructured grids are not axisymmetric, but are periodic with respect to 60° rotation and reflection symmetric with respect to planes with circumferential angles, which are multiples of 30°. The circumferential angle is computed as $\phi = tan^{-1}\left(\frac{z}{y}\right)$. The fine 360° grid has $125,946,869$ nodes, $22,732,800$ prisms, and $113,664,000$ hexahedra. The fine surface grid over the cylinder portion of the viscous boundary is composed of $128,000$ quadrilateral faces, 800 quadrilateral faces in the streamwise direction and 160 quadrilateral faces in the circumferential direction, and $25,600$ equilateral triangular faces form the surface grid over the hemisphere. The volume grid is extended by 888 elements from the hemisphere-cylinder surface

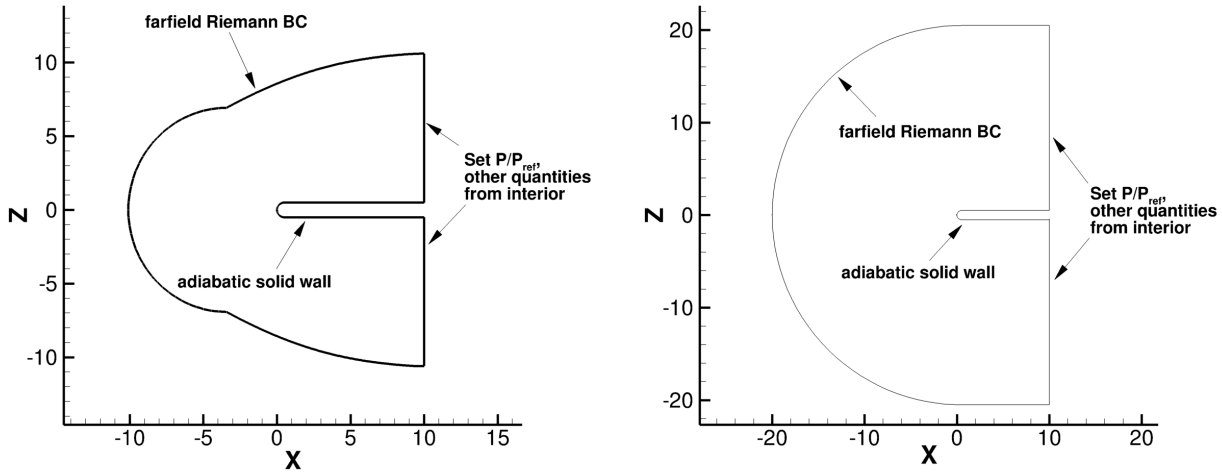

(a) Unstructured grid domain.

(b) Structured grid domain.

Figure 12. Vertical eddy viscosity variation

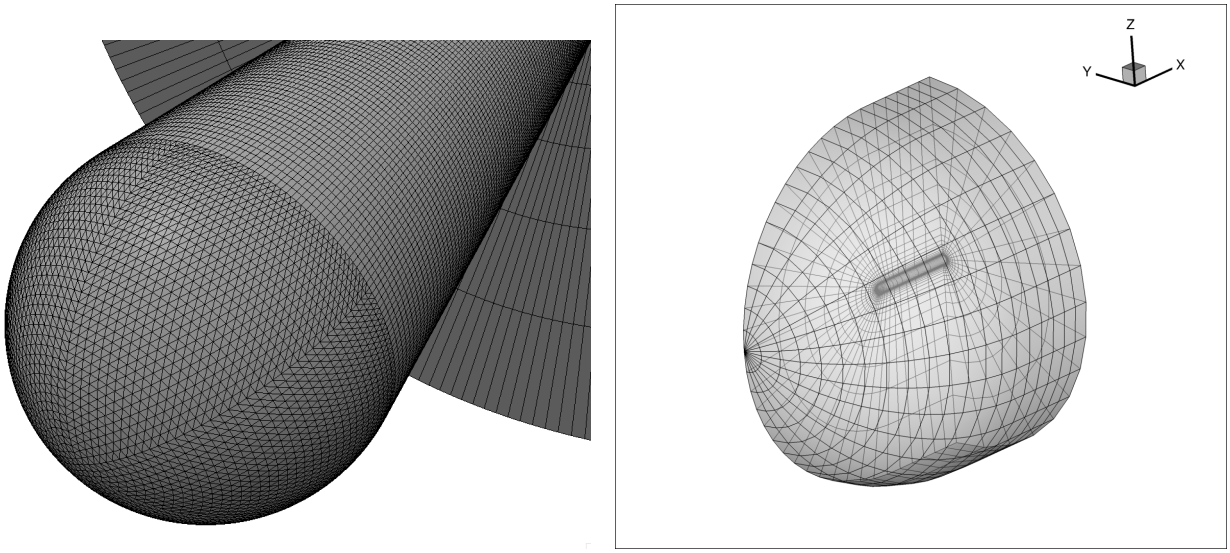

(a) Unstructured surface grid.

(b) Structured volume grid.

Figure 13. 3D hemisphere-cylinder configuration grids

to the farfield boundary. The mesh spacing near the surface corresponds to $z^+ = 0.5$. The corresponding medium grid has $15,858,075$ nodes, $2,841,600$ prisms, $14,208,000$ hexahedral volume elements, $32,000$ quadrilateral and $6,400$ triangular faces at the viscous surface. The coarse grid has $2,010,998$ nodes, $355,200$ prisms, $1,776,000$ hexahedral volume elements, $8,000$ quadrilateral and $1,600$ triangular faces at the viscous surface. The coarse surface grid is shown in Figure 13(a). In reported computations, USM3D uses 60° grids with two symmetry boundaries, employing one sixth of volume elements associated with 360° grids; FUN3D computes on the 360° grids.

CFL3D solutions are computed on a family of structured grids with polar singularity. A family of six axisymmetric 180° grids ranging from the coarsest $6 \times 10 \times 5$ grid to the finest $161 \times 289 \times 129$ grids have been generated. The grid dimensions represent the numbers of nodes in the streamwise, normal, and circumferential directions, respectively.

Within the family, grids have been generated recursively, starting from the finest grid. Each coarser grid in the family is derived from the preceding finer grid by removing every-other grid plane in each dimension. Structured grids used in these computations have significantly fewer elements than unstructured grids; the finest structured grid has only $11,796,480$ hexahedral elements in the equivalent 360° grid (the prismatic elements around the pole are considered as degenerated hexahedra), less that one tenth of the elements on the finest unstructured grid. The near-surface mesh spacing on the finest structured grid corresponds to $z^+ = 0.8$. The 180° $21 \times 37 \times 17$ grid is shown in Figure 13(b).

C. Results

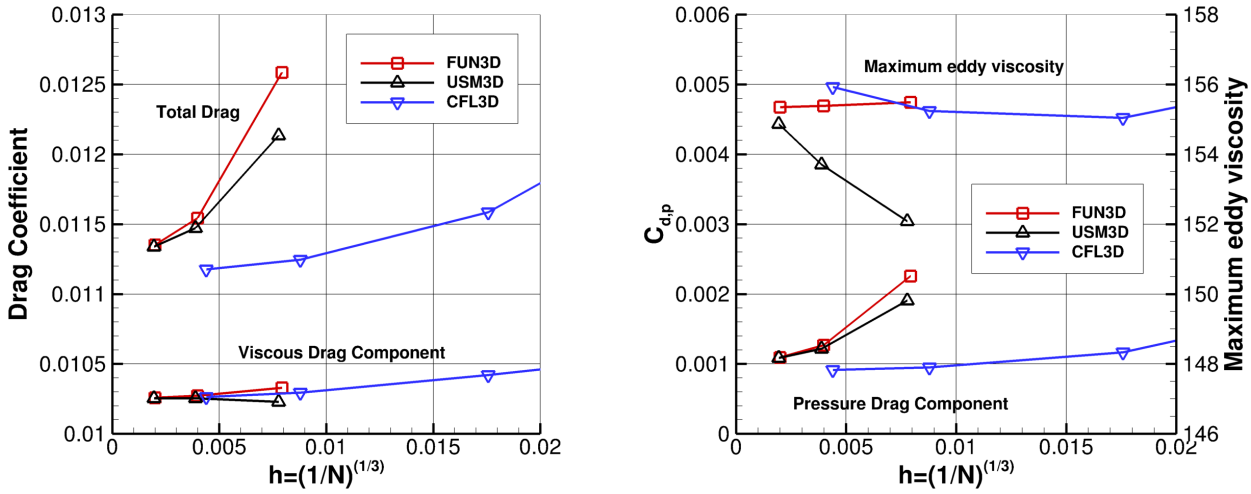

(a) Total and viscous drag.

(b) Pressure drag and eddy viscosity.

Figure 14. Grid convergence of drag and eddy viscosity

Grid convergence of the total drag, viscous drag, pressure drag, and the maximum eddy viscosity is shown in Figure 14. All drag components appear converging in grid refinement to the same limit. FUN3D and USM3D drag components computed on unstructured grids are closer to each other than to the corresponding CFL3D components computed on structured grids. The difference between total drag coefficients on the finest grids in the families is less than 2 drag counts (less than 2%). The difference between drag coefficients computed by FUN3D and USM3D on the finest unstructured grid is an order of magnitude smaller. The difference is mostly due to the variation in the pressure drag, which is a minor (less than 10%) contributor to the total drag for this case. The corresponding variation in the viscous drag coefficients is less than 0.1 count. The grid convergence of the maximum eddy viscosity is less clear. The FUN3D values appears to be approaching 155 whereas the USM3D and CFL3D values appear to be approaching 157. The relative differences in the asymptotic values are small, less than 1.3%.

Figure 15 presents surface pressure and skin friction variations along the streamwise (x-)direction. The numerical solutions computed on the finest grids for the USM3D and CFL3D solutions are shown along the surface line corresponding to the 30° circumferential angle. The values shown for the FUN3D solution include all angles. The experimental values of the pressure coefficient[39] are also shown in Figure 15(a). All computational solutions overplot in these global views; the surface pressure profile reasonably matches the experimental data.

Figure 16 shows variations of pressure, eddy viscosity, and streamwise velocity in the radial direction. The data are taken from the finest grid line (approximately) orthogonal to the surface and attached to the surface at the interface between the hemisphere and the cylinder ($x = 0.5$). All solutions correspond to the $\phi = 30^\circ$ circumferential angle. All solutions show a close agreement in these global views.

Figures 17 and 18 show circumferential variations of pressure and skin friction in FUN3D and USM3D solutions at $x = 0.25$. The axisymmetric CFL3D solutions have no circumferential variations and are shown for reference. On each grid, FUN3D and USM3D pressure plots are closer to each other than to CFL3D pressure plots. On the finest grids, code-to-code variations are less that 0.5%. In grid refinement, the CFL3D skin friction coefficient converges

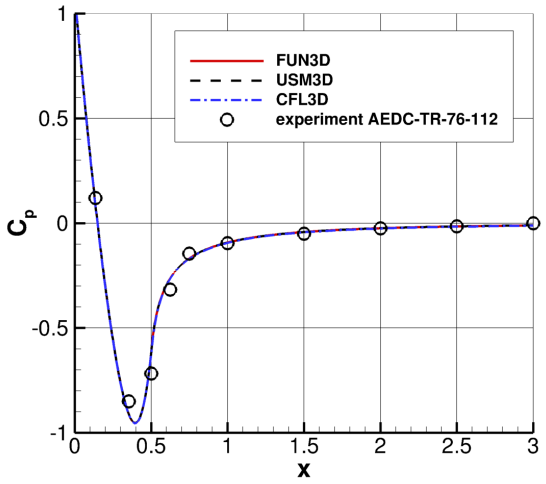

(a) Pressure coefficient.

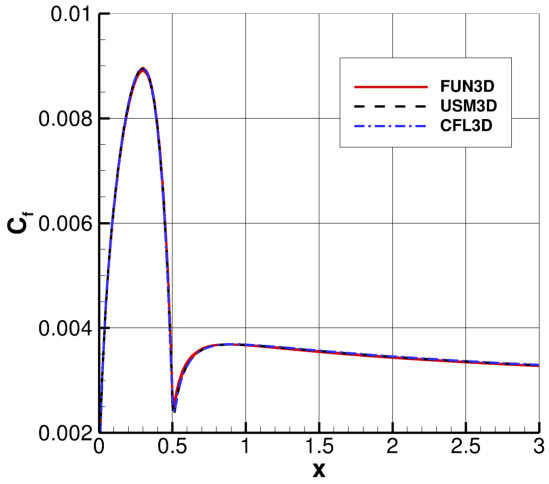

(b) Skin friction coefficient.

Figure 15. Axial variation of pressure and skin friction

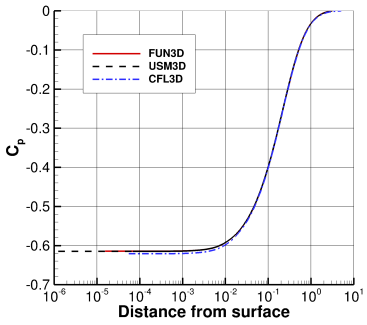

(a) Pressure coefficient.

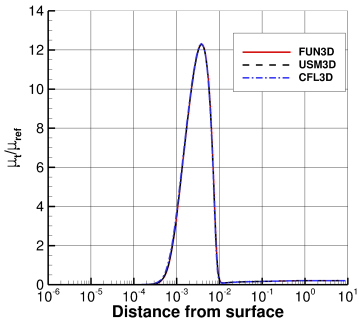

(b) Eddy Viscosity.

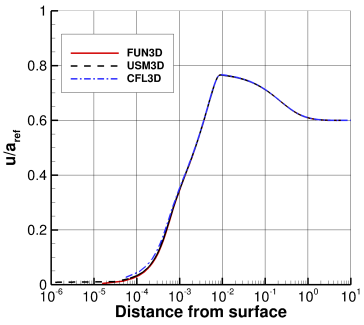

(c) Streamwise velocity.

Figure 16. Radial variation of pressure, eddy viscosity, and streamwise velocity

from higher values, while the FUN3D and USM3D skin friction profiles converge from lower values. On the finest grids, the USM3D skin friction is closer to the CFL3D value than the FUN3D skin friction; the maximum variation between finest-grid solutions does not exceed 1%. On each grid, the maximum variations are observed near boundaries of 60° sectors, where there are abrupt changes in the surface grid triangulation. These variations are decreasing in grid refinement.

Grid convergence for the pressure coefficient is shown in Figure 19 at three locations, $x = 0.25$, $x = 0.5$, and $x = 1.5$. The FUN3D and USM3D values are taken at a line corresponding to $\phi = 30^\circ$. The code-to-code pressure-coefficient variation on the finest grid is less than 1%.

V. Supersonic Flow in a Square Duct

Reference solutions for a supersonic flow in a square duct computed by FUN3D and USM3D are presented in this section. The solutions correspond to the case described in 3D Modified Supersonic Square Duct Validation Case in the Cases and Grids for Turbulence Model Numerical Analysis section of the TMR website. These reference solutions

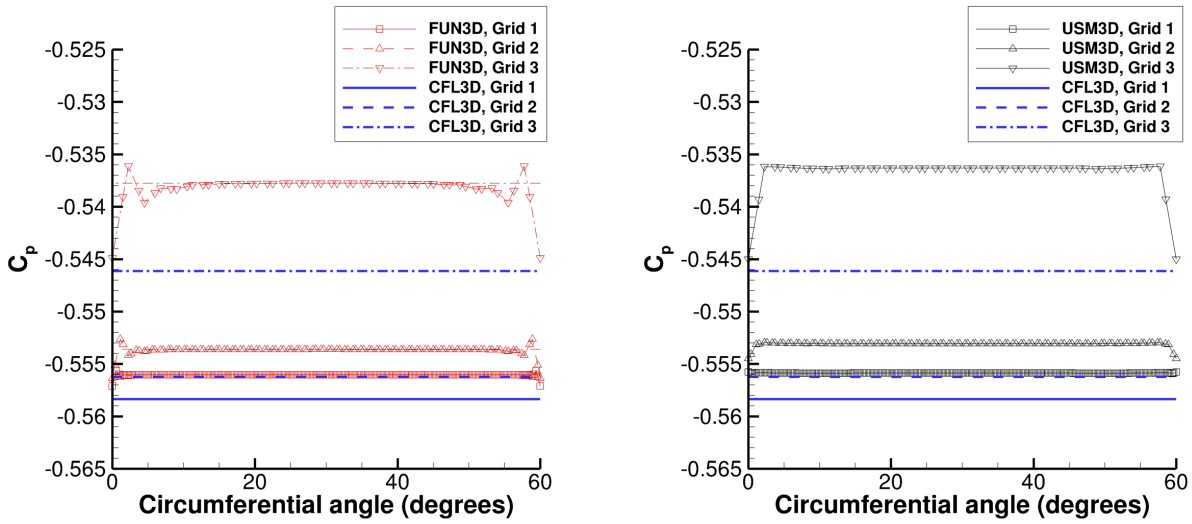

(a) FUN3D vs CFL3D.

(b) USM3D vs CFL3D.

Figure 17. Circumferential variation of surface pressure

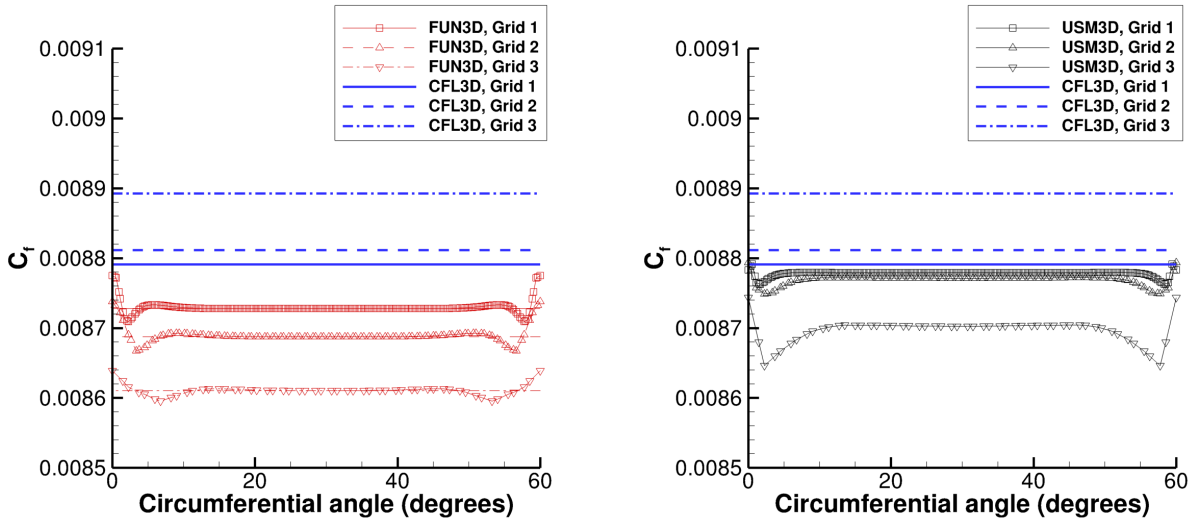

(a) FUN3D vs CFL3D.

(b) USM3D vs CFL3D.

Figure 18. Circumferential variation of skin friction

can be used for verification of RANS solvers with the SA-QCR2000 turbulence model. [5] A grid convergence study as well as comparisons with an experimental study[40] are shown.

A. Geometry, Boundary Conditions, and Flow Parameters

The experiment utilizes a constant area square duct of height and width $D = 25.4mm$. The primary feature of this case is the flow in the corners. In such cases, turbulent anisotropies are important because normal stress differences induce flow behavior that cannot be captured with models based on the Boussinesq assumption. The experimental measurements were conducted at the stations located $40D$ and $50D$ downstream of the duct orifice.

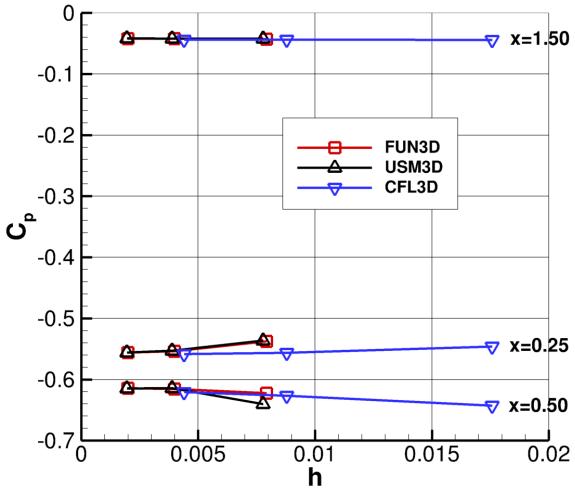

Figure 19. Grid convergence of pressure coefficient

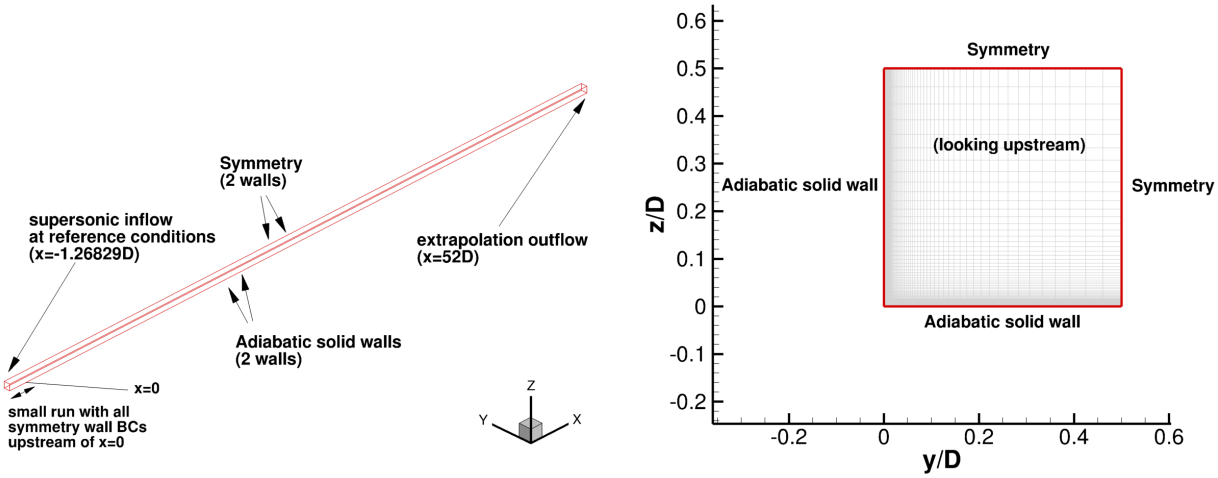

(a) Far view.

(b) Near view.

Figure 20. Boundary conditions for 3D supersonic flow in a square duct

In the simulations, the coordinate system origin is set at the lower-left corner of the front section of the duct. The positive direction of the x-axis is the streamwise direction along the duct. The computational domain is extended upstream as $-1.26829D < x < 52D, 0 < y < 0.5D, 0 < z < 0.5D$, to allow for a small run of symmetry boundary conditions prior to the orifice of the duct. The set of boundary conditions is illustrated in Figures 20. Adiabatic-wall conditions are set at the duct left and bottom boundaries. Supersonic inflow conditions are set at $x = -1.26829D$ corresponding to free stream. Supersonic outflow is set at $x = 52D$. Symmetry conditions are used on the right ($y = 0.5D$) and top ($z = 0.5D$) boundaries and on all boundaries at $-1.26829D < x < 0$. Due to use of symmetry boundary conditions, only one quarter of the duct is computed.

The flow conditions corresponding to the experiment are as follows. The Reynolds number per D is $Re = 508,000$, the reference Mach number is $M_{ref} = 3.9$, and the reference temperature is $T_{ref} = 520°$ Rankine.

B. Grids

The computations are performed on four nested structured 3D grids, ranging from $673 \times 193 \times 193$ (fine grid 1) to $337 \times 97 \times 97$ (medium grid 2) to $169 \times 49 \times 49$ (coarse grid 3) to $85 \times 25 \times 25$ (extra-coarse grid 4).. The grid dimensions represent nodes in the streamwise, spanwise, and vertical directions, respectively. Each coarser grid is exactly every-other-plane of the next finer grid. The grids are stretched in the two wall-normal directions. The finest grid has the minimum spacing at the wall of $y = 8.5 \times 10^{-6}$. Figure 21 shows a cross-section view of the $337 \times 97 \times 97$ grid.

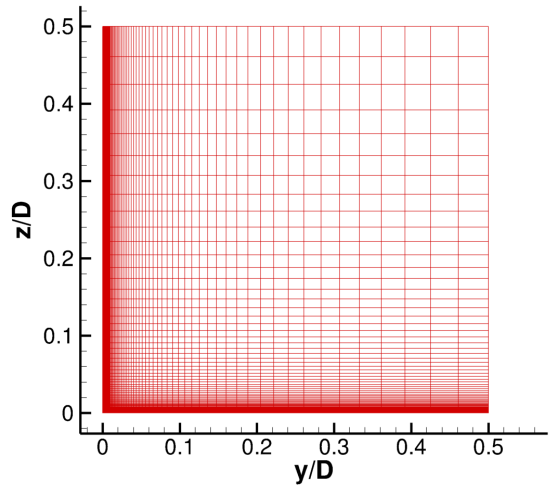

Figure 21. 3D supersonic flow in a square duct: upstream view on $337 \times 97 \times 97$ grid

C. Results

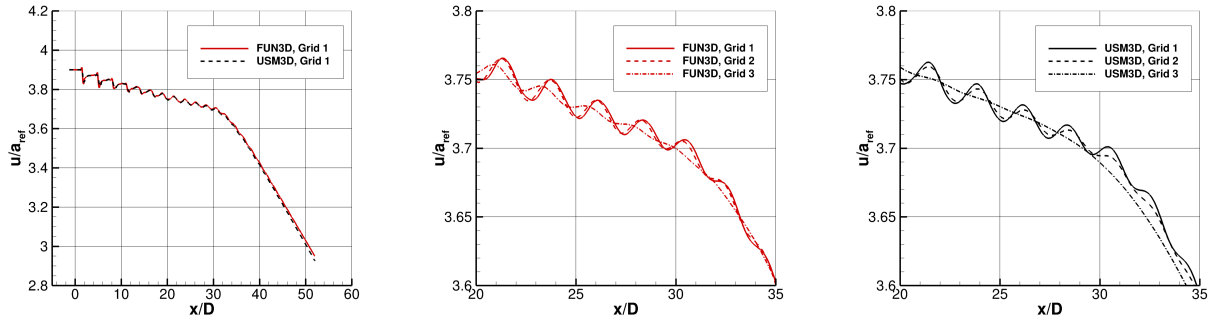

(a) Global view.

(b) FUN3D, close view.

(c) USM3D, close view.

Figure 22. Centerline velocity: global variation

Variations of the centerline velocity normalized by the reference (inflow) speed of sound are shown in Figure 22. The USM3D and FUN3D profiles on the finest grid are hardly distinguishable in the global view (Figure 22 (a)). Solutions on fine, medium, and coarse grids are shown in Figures 22 (b) and (c). The coarse grid (Grid 3) is clearly not adequate to accurately capture the centerline velocity oscillations; for this reason, the extra-coarse grid solution is not shown. Solutions obtained by FUN3D and USM3D on the fine and medium grids are similar. Judging by relative differences between solutions on fine and medium grids, FUN3D provides a better resolution in the back part of the duct than USM3D.

Figure 23 shows the centerline velocities computed on different grids at the cross-sections corresponding to $x = 40D$ and $x = 50D$. On the finest grid, the FUN3D and USM3D velocity values are less than 1% apart, but appear converging to different limits. The centerline velocity values computed by FUN3D are higher than the corresponding values computed by USM3D on all grids and the code-to-code variations are not reducing in grid refinement.

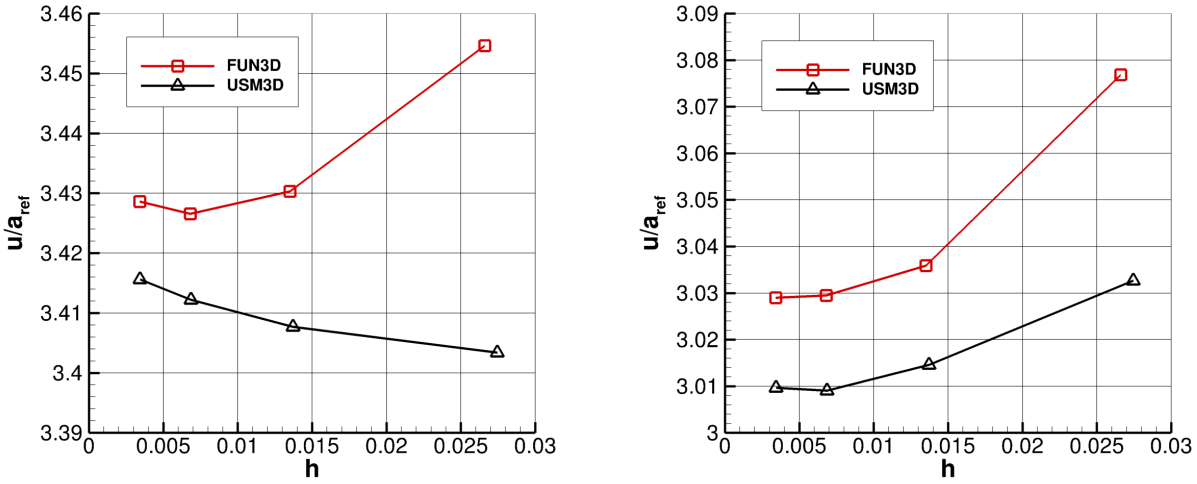

(a) $x = 40D$.

(b) $x = 50D$.

Figure 23. Centerline velocity: grid convergence

The streamwise velocity profiles normalized by the local centerline velocity, u/u_{CL}, computed on coarse, medium, and fine grids are compared with the experiment in Figure 24. Figures 24 (a) and (b) compare the velocity profiles at $x = 40D$ for the diagonal $y = z$ and vertical $y = 0.5D$ cuts across the duct. Corresponding comparisons at $x = 50D$ are shown in Figures 24 (c) and (d). The numerical profiles on all grids are essentially over-plotted in this global view. The only noticeable departure corresponds to the slight deviation of the USM3D coarse-grid profile from the others in the low portion of the duct $0.1 < 2z/D < 0.4$.

The skin friction profiles along $y = 0$ and $x = 40D$ and $x = 50D$ are shown in Figures 25 and 26, respectively. The skin friction coefficients on the medium and fine grids overplot below $2z/D \leq 0.8$. The skin friction levels near $2z/D = 1$ monotonically decrease on finer grids. Overall, the computations and the experiment are in a reasonable agreement except for the skin friction values at $x = 50D$ in the immediate vicinity of the corner, where the computations under-predict the experimental measurements. Consistent with the finest grid-variations of centerline velocity noted earlier, the FUN3D skin friction values are slightly higher than the USM3D values.

VI. Concluding Remarks

Grid convergence studies have been conducted to establish benchmark solutions for three turbulent flows in three dimensions (3D). The study cases are two subsonic external flows — around a 3D bump and a hemisphere-cylinder configuration — and a supersonic internal flow in a square duct. These test cases originated from previous comparisons on the Turbulence Modeling Resource (TMR) website developed at NASA Langley Research Center (LaRC). The TMR website supports the Computational Fluid Dynamics (CFD) community with resources for validation and verification of turbulence models. The steady solutions computed in the current study establish new 3D Reynolds Averaged Navier Stokes (RANS) verification cases. The RANS formulation for the external flows uses the "negative" variant of the standard Spalart-Allmaras (SA) model with a linear eddy viscosity model. The formulation for the duct flow uses the SA model with a nonlinear eddy viscosity model based on a quadratic constitutive relation (QCR) extension. The study involves three widely-used practical CFD codes developed at NASA LaRC – FUN3D, CFL3D, and USM3D – and families of consistently refined grids intended to enable high resolution on the finer grids. The codes use different discretization approaches and iterative solution methods. To eliminate iterative errors, all solutions on all grids have converged to near machine-zero residual levels. Although turbulence model validation is not the focus of

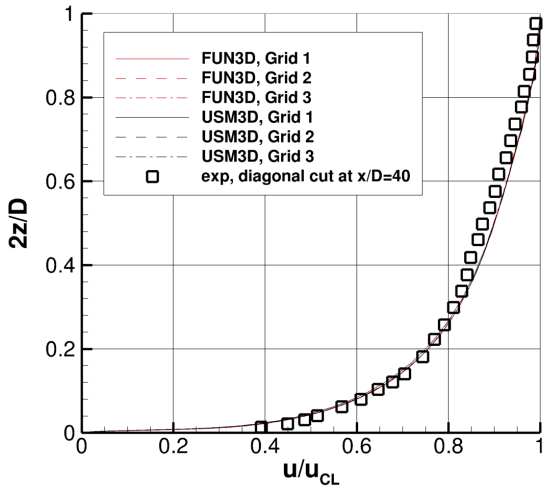

(a) Diagonal cut, $x = 40D$.

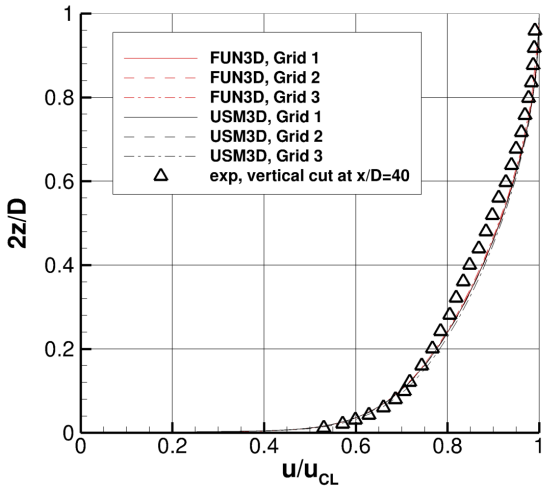

(b) Vertical cut, $x = 40D$.

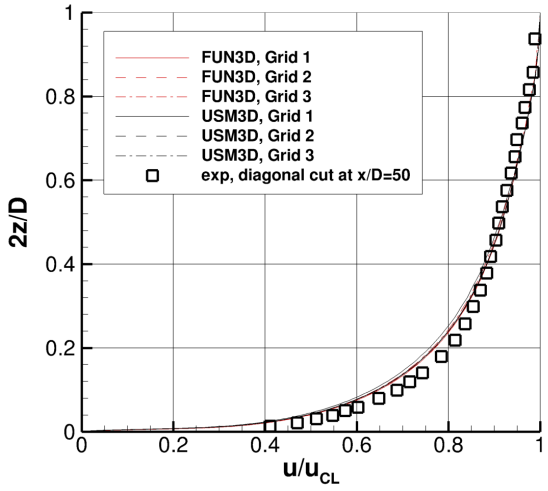

(c) Diagonal cut, $x = 50D$.

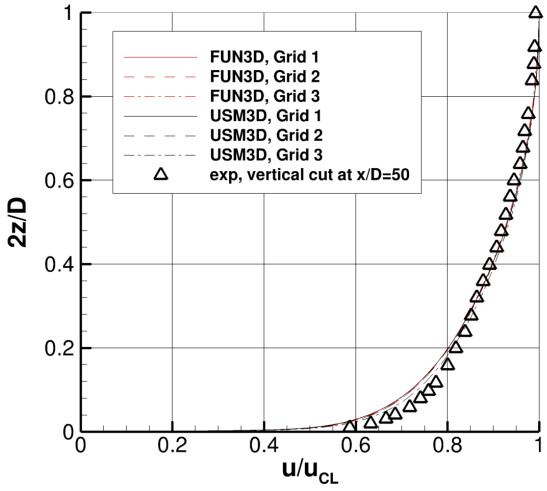

(d) Vertical cut, $x = 50D$.

Figure 24. Streamwise velocity profile

the paper, for the hemisphere-cylinder configuration and duct cases, the reference solutions have been compared with available experimental data. The main thrust of the paper is assessing variations between CFD solutions computed with different codes in grid refinement. The assessment includes two characteristics: (1) relative code-to-code variations of aerodynamic quantities computed on the finest available grids and (2) variations in the limit of grid refinement.

The following general observations have been reported.

1. All three solutions show close agreement in predicting the external flows (3D bump and hemisphere-cylinder configuration). The code-to-code variations between drag and lift coefficients computed on the finest grids do not exceed 2%. The coefficients appear to converge to the same limit in grid refinement. There is a small ambiguity about the convergence limit of the maximum eddy viscosity for the flow over the hemisphere-cylinder configuration. The curves characterizing variations of the surface pressure and skin friction in different fine-grid solutions overplot. The curves of volume variations of various solution components also overplot. Local

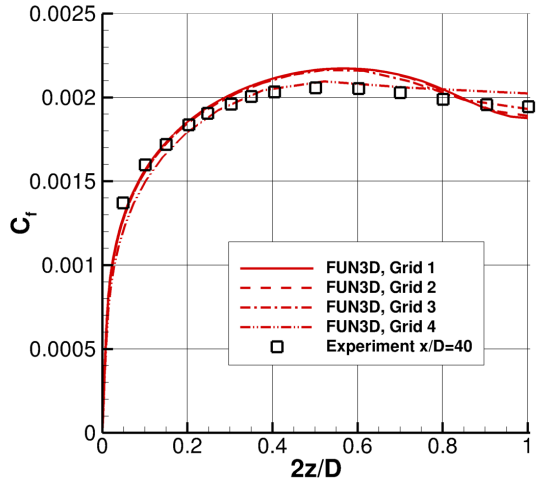

(a) FUN3D.

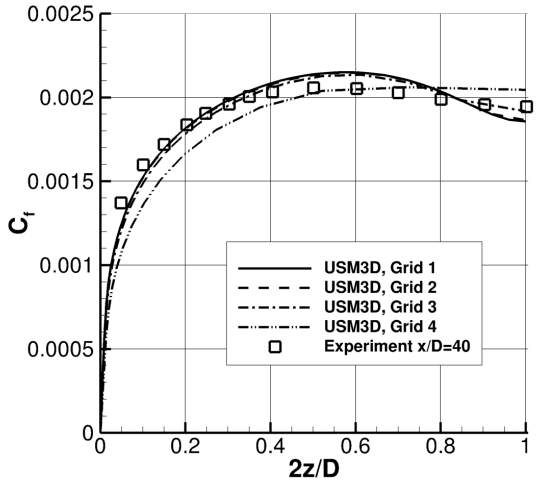

(b) USM3D.

Figure 25. Skin friction profile at $x = 40D$

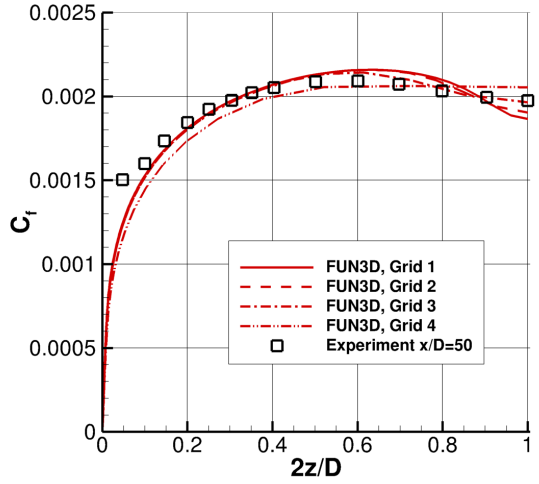

(a) FUN3D.

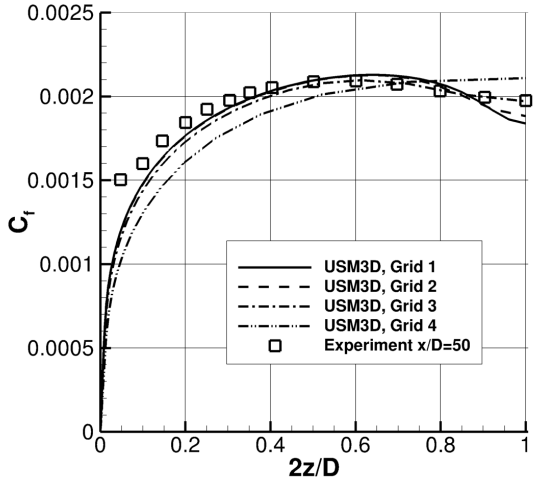

(b) USM3D.

Figure 26. Skin friction profile at $x = 50D$

solution characteristics, such as local pressure, computed with different codes also converge to the same limit in grid refinement. For the axisymmetric flow around the hemisphere-cylinder configuration, unstructured-grid solutions show some circumferential variations. The variations are caused by asymmetrical surface triangulation typical for unstructured grids that eliminate the polar singularities associated with structured grids. These variations are small, do not exceed a few per cent, and decrease in grid refinement. The reference solutions for external flows show reasonable agreement with available experimental data.

2. Only USM3D and FUN3D have been used to compute the supersonic duct flow. The solutions on the finest grids are close to each other, show small grid-to-grid variations in velocity and skin friction on the two finest grids,

and show reasonable agreement with experimental data. However, a close inspection of the local centerline velocities reveals that while the relative code-to-code differences are small, less than 1%, the grid convergence trend is uncertain. Because the code-to-code variations are not decreasing in grid refinement, it appears the centerline velocities do not converge to the same limit in grid refinement. There are no satisfactory explanations for this observation. Additional investigations are required to understand the source of this discrepancy.

Acknowledgment

The authors are grateful for the help in grid generation and processing received from Dr. H. Nishikawa (NIA) and Dr. E. B. Parlette (ViGYAN). The first author acknowledges support from NASA Cooperative Agreement NNL09AA00A.

References

[1]"Turbulence Modeling Resource Website," `http://turbmodels.larc.nasa.gov`.

[2]Rumsey, C. L., Smith, B. R., and Huang, G. P., "Description of a Website Resource for Turbulence Modeling Verification and Validation," AIAA Paper 2010-4742, 2010.

[3]Spalart, P. R. and Allmaras, S. R., "A One-Equation Turbulence Model for Aerodynamic Flows," *Recherche Aerospatiale*, , No. 1, 1994, pp. 5–21.

[4]Allmaras, S. R., Johnson, F. T., and Spalart, P. R., "Modifications and Clarifications for the Implementation of the Spalart-Allmaras Turbulence Model," *Seventh International Conference on Computational Fluid Dynamics*, Big Island, Hawaii, 2012.

[5]Spalart, P. R., "Strategies for Turbulence Modelling and Simulation," *International Journal of Heat and Fluid Flow*, Vol. 21, 2000, pp. 252–263.

[6]AIAA G-007-1998, "Guide for Verification and Validation of Computational Fluid Dynamics Simulations," 2002.

[7]Oberkumpf, W. L. and Roy, C. J., *Verification and Validation in Scientific Computing*, Cambridge University Press, 2010.

[8]Park, M. A., Laflin, K. R., Chaffin, M. S., Powell, N., and Levy, D. W., "CFL3D, FUN3D, and NSU3D Contributions to the Fifth Drag Prediction Workshop," *Journal of Aircraft*, Vol. 51, 2014, pp. 1268–1283.

[9]Lee-Rausch, E. M., Rumsey, C. L., and Park, M. A., "Grid-Adapted FUN3D Computations for the Second High Lift Prediction Workshop," AIAA 2014-2395, 2014.

[10]Bartels, R., Vatsa, V. N., Carlson, J.-R., and Mineck, R., "FUN3D Grid Refinement and Adaptation Studies for the Ares Launch Vehicle," AIAA 2010-4372, 2010.

[11]Chwalowski, P. and Heeg, J., "FUN3D Analyses in Support of the First Aeroelastic Prediction Workshop," AIAA 2013-0785, 2013.

[12]Park, M. A., "Low Boom Configuration Analysis with FUN3D Adjoint Simulation Framework," AIAA 2011-3337, 2013.

[13]Gnoffo, P. A., Wood, W. A., Kleb, B., Alter, S. J., Padilla, J., and White, J. A., "Functional Equivalence Acceptance Testing of FUN3D for Entry, Descent, and Landing Applications," AIAA 2013-2558, 2013.

[14]Vatsa, V. N., Khorrami, M. R., Park, M. A., and Lockard, D. P., "Aeroacoustic Simulation of Nose Landing Gear on Adaptive Unstructured Grids with FUN3D," AIAA 2013-2071, 2013.

[15]Nielsen, E. J. and Diskin, B., "Discrete Adjoint-Based Design for Unsteady Turbulent Flows on Dynamic Overset Unstructured Grids," *AIAA J.*, Vol. 51, No. 6, 2013, pp. 1355–1373.

[16]Diskin, B., Thomas, J. L., Nielsen, E. J., Nishikawa, H., and White, J. A., "Comparison of Node-Centered and Cell-Centered Unstructured Finite-Volume Discretizations: Viscous Fluxes," *AIAA J.*, Vol. 48, No. 7, July 2010, pp. 1326–1338.

[17]Diskin, B. and Thomas, J. L., "Comparison of Node-Centered and Cell-Centered Unstructured Finite-Volume Discretizations: Inviscid Fluxes," *AIAA J.*, Vol. 49, No. 4, 2011, pp. 836–854.

[18]Diskin, B. and Thomas, J. L., "Comparison of Node-Centered and Cell-Centered Unstructured Finite-Volume Discretizations: Inviscid Fluxes. (Composition erratum)," *AIAA J.*, Vol. 51, No. 1, 2013, pp. 277–277.

[19]Pandya, M., Frink, N., Abdol-Hamid, K., Samareh, J., Parlette, E., and Taft, J., "Enhancements to TetrUSS for NASA Constellation Program," *Journal of Spacecraft and Rockets*, Vol. 49, No. 4, 2012, pp. 617–631.

[20]Bauer, S. X., Krist, S. E., and Compton, W. B., "Generation of the Ares I-X Flight Test Vehicle Aerodynamic Data Book and Comparison To Flight," AIAA 2011-0011, 2011.

[21]Abdol-Hamid, K. S., Ghaffari, F., and Parlette, E. B., "Ares I Vehicle Computed Turbulent Ascent Aerodynamic Data Development and Analysis," *Journal of Spacecraft and Rockets*, Vol. 49, No. 4, 2012, pp. 296–608.

[22]Green, B. E., "Computational Prediction of Nose-Down Control for F/A-18E at High Alpha," *Journal of Aircraft*, Vol. 45, No. 5, 2008, pp. 296–608.

[23]Hooker, J. R., Wick, A., Zeune, C., and Agelastos, A., "Over Wing Nacelle Installations for Improved Energy Efficiency," AIAA 2013-2920, 2013.

[24]Pandya, M. J., Diskin, B., ames L. Thomas, and Frink, N. T., "Improved Convergence and Robustness of USM3D Solutions on Mixed Element Grids," AIAA 2015-1747, 2015.

[25]Pandya, M. J., Diskin, B., ames L. Thomas, and Frink, N. T., "Assessment of Preconditioner for a USM3D Hierarchical Adaptive Nonlinear Method (HANIM)," AIAA 2016-????, 2016.

[26]Courant, R. and Hilbert, D., *Methods of Mathematical Physics*, Interscience, New York, 1962.

[27]Holmes, D. G. and Connell, S. D., "Solution of the 2D Navier-Stokes equations on unstructured adaptive grids," *9th AIAA Computational Fluid Dynamics Conference*, AIAA Paper 89-1932, Washington, DC, 1989.

[28]Rausch, R. D., Batina, J. T., and Yang, H. T., "Spatial adaptation procedures on unstructured meshes for accurate unsteady aerodynamic flow computation," *AIAA J.*, Vol. 30, No. 5, 1992, pp. 1243–1251.

[29]Frink, N. T., "Assesment of an unstructured-grid method for predicting 3-D turbulent viscous flows," *34th AIAA Aerospace Science Meeting and Exhibit*, AIAA Paper 96-0292, Reno, 1996.

[30]Haselbacher, A. and Blazek, J., "Accurate and Efficient Discretization of Navier-Stokes Equations on Mixed Grids," *AIAA J.*, Vol. 38, No. 11, 2000, pp. 2094–2102.

[31]Mitchell, C. R., "Improved Reconstruction Schemes for the Navier-Stokes Equations on Unstructured Meshes," AIAA 1994-0642, 1994.

[32]Frink, N. T., "Tetrahedral Unstructured Navier-Stokes Method for Turbulent Flows," *AIAA J.*, Vol. 36, No. 11, 1998, pp. 1975–1982.

[33]Rumsey, C. L., "CFL3D Contribution to the AIAA Supersonic Shock Boundary Layer Interaction Workshop," NASA/TM 2010-216858, 2010.

[34]Heeg, J., "Overview and Lessons Learned from the Aeroelastic Prediction Workshop," AIAA 2013-1798, 2013.

[35]Park, M. A., Lee-Rausch, E. M., and Rumsey, C. L., "FUN3D and CFL3D Computations for the First High Lift Prediction Workshop," AIAA 2011-0936, 2011.

[36]Anderson, W. K., Thoma, J. L., and van Leer, B., "Comparison of Finite Volume Flux Vector Splittings for the Euler Equations," *AIAA Journal*, Vol. 24, No. 9, 1986, pp. 1453–1460.

[37]Burg, C. O. E., "Higher Order Variable Extrapolation For Unstructured Finite Volume RANS Flow Solvers," AIAA 2005-4999, 2005.

[38]White, F. M., *Viscous Fluid Flow*, McGraw-Hill, 2nd ed., 1991.

[39]Tsieh, T., "An Investigation of Separated Flow About a Hemisphere-Cylinder at 0- to 19-Deg Incidence in the Mach Number Range from 0.6 to 1.5," AEDC-TR-76-112, 1976.

[40]Davis, D. O., Gessner, F. B., and Kerlick, G. D., "Experimental and numerical investigation of supersonic turbulent flow through a square duc," *AIAA J.*, Vol. 24, No. 9, 1986, pp. 1508–1515.